

# Determination of atmospheric parameters to estimate global radiation in areas of complex topography: Generation of global irradiation map

F.J. Batlles<sup>a,\*</sup>, J.L. Bosch<sup>a</sup>, J. Tovar-Pescador<sup>b</sup>, M. Martínez-Durbán<sup>c</sup>,  
R. Ortega<sup>d</sup>, I. Miralles<sup>e</sup>

<sup>a</sup> Dpto. Física Aplicada, Universidad de Almería, 04120 Almería, Spain

<sup>b</sup> Dpto. Física, Universidad de Jaén, 23071 Jaén, Spain

<sup>c</sup> Dpto. Ingeniería Lenguajes y Computación, Universidad de Almería, 04120 Almería, Spain

<sup>d</sup> Dpto. Edafología y Química Agrícola, Universidad de Almería, 04120 Almería, Spain

<sup>e</sup> Dpto. Edafología y Química Agrícola, Universidad de Granada, 28071 Granada, Spain

Received 19 October 2006; accepted 4 June 2007

Available online 20 August 2007

## Abstract

Incoming shortwave solar radiation is an important parameter in environmental applications. A detailed spatial and temporal analysis of global solar radiation on the earth surface is needed in many applications, ranging from solar energy uses to the study of agricultural, forest and biological processes. At local scales, the topography is the most important factor in the distribution of solar radiation on the surface. The variability of the elevation, the surface orientation and the obstructions due to elevations are a source of great local differences in insolation and, consequently, in other variables as ground temperature. For this reason, several models based on GIS techniques have been recently developed, integrating topography to obtain the solar radiation on the surface.

In this work, global radiation is analyzed with the Solar Analyst, a model implemented on ArcView, that computes the topographic parameters: altitude, latitude, slope and orientation (azimuth) and shadow effects. Solar Analyst uses as input parameters the diffuse fraction and the transmittance. These parameters are not usually available in radiometric networks in mountainous areas. In this work, a method to obtain both parameters from global radiation is proposed. Global radiation data obtained in two networks of radiometric stations is used: one located in Sierra Mágina Natural Park (Spain) with 11 stations and another one located on the surroundings of Sierra Nevada Natural Park (Spain) with 14 stations. Daily solar irradiation is calculated from a digital terrain model (DTM), the daily diffuse fraction,  $K$ , and daily atmospheric transmittivity,  $\tau$ . Results provided by the model have been compared with measured values. An overestimation for high elevations is observed, whereas low altitudes present underestimation. The best performance was also reported during summer months, and the worst results were obtained during winter. Finally, a yearly global solar irradiation map has been produced for the studied zone.

© 2007 Elsevier Ltd. All rights reserved.

**Keywords:** Global solar radiation; DTM; Radiation map

## 1. Introduction

Incoming solar radiation, through its influence over the energy and water balances of the earth surface, affects pro-

cesses like air and soil heating, evapotranspiration, photosynthesis, wind, snow thawing, etc. Therefore, this knowledge is important in diverse fields as hydrology [1], climatology [1], biologic processes [2], energy applications [3–6] or agriculture [2]. Since solar radiation is the energy source for photosynthesis and evapotranspiration, its supply is paramount to the potential production and well

\* Corresponding author. Tel.: +34 950 015914; fax: +34 950 015477.

E-mail address: [fbatlles@ual.es](mailto:fbatlles@ual.es) (F.J. Batlles).

## Nomenclature

$I_{sc}$	solar constant (118.08 MJ/m <sup>2</sup> day)	$D_{\theta_z, \psi}$	diffuse radiation for one sky sector (MJ/m <sup>2</sup> day).
$K$	daily diffuse fraction	$B_{\theta_z, \psi}$	direct radiation for one sun map sector (MJ/m <sup>2</sup> day).
$k_t$	daily clearness index	$V_{\theta_z, \psi}$	proportion of visible sky for sky sector
$\tau$	daily atmospheric transmittivity	$S_{\theta_z, \psi}$	proportion of diffuse radiation originating in given sector relative to all sectors
$\theta_z$	solar zenith angle	$\Delta$	time interval duration
$\psi$	azimuth solar angle	$S_{\theta_z, \psi}$	time duration represented by sky sector
$H_g$	daily global solar irradiance (MJ/m <sup>2</sup> day)	$\xi_{\theta_z, \psi}$	gap fraction for sun map sector
$H_b$	daily direct solar radiation (MJ/m <sup>2</sup> day)	$R_n$	global normal radiation, obtained from direct radiation for every sector
$H_d$	daily diffuse solar irradiation (MJ/m <sup>2</sup> day)	MBE	mean bias error
$m_\theta$	optical air mass	RMSE	root mean square error
$\theta_s$	surface zenith angle		
$\psi_s$	surface azimuth angle		
$\theta$	angle between centroid of sky sector and axis normal to surface		

being of crops and forest stands. In particular, canopy photosynthesis (and, thus, biomass production) depends on the coupling between the photosynthetic response of leaves and the distribution of radiation on these elements [7]. For that reason, daily global irradiation is the main input parameter for agronomic, ecologic and hydrologic models [7–9]. For most of these applications, global radiation measures are needed over wide regions, for long time periods and with a high spatial resolution.

Usually, solar radiation estimation methods are based on ground measures obtained from dispersed radiometric networks. Interpolation/extrapolation techniques, applied to the measured data, are performed to estimate the solar radiation at points located away from the stations. These interpolation/extrapolation methodologies are valid in places where the radiation variability is not very high but are not suitable techniques if the area between the measuring stations presents a dissimilar radiative behaviour, as happens in terrains with a very complex topography [5]. In these circumstances, solar radiation estimation has to be performed by means of very dense radiometric nets with high cost and maintenance difficulties [10]. Many natural parks have very complex topographies and specific solutions have to be adopted because it is not possible to characterize these areas with the usual methods described above.

Apart from daily and seasonal cycles, clouds and topography are the major modulators of solar irradiation reaching the earth surface [11]. At local scales, topography is a very important driver of solar radiation at ground level. Variability in elevation, azimuth and horizon obstruction due to adjacent elevations results in strong local radiation gradients and, consequently, influences a great number of climatic variables (surface and soil temperature, evapotranspiration, humidity, etc.) In several applications, variations in incident solar radiation with topography are of major importance. For example, in the northern hemisphere, south oriented hillsides collect much more radia-

tion than north oriented slopes, having different energy exchanges on their surfaces.

The correlation between the measured data of global radiation diminishes linearly [12,13] or logarithmic [14] with distance. This diminution is most important in sites with great topographic variability [15]. This is the reason why ground radiometric networks are not able to describe the spatial variations: generally, stations are too dispersed to account for this variability. In the last years, the use of geographic information systems (GIS), incorporating a DTM has contributed to solve this difficulty and improved solar radiation estimation. GIS work easily with solar radiation estimation models, being able to calculate the solar radiation on surface data for all types of terrains.

Solar Analyst, one of the most used models to calculate solar radiation by means of GIS techniques, requires values of the diffuse fraction and the transmittivity of the atmosphere as input parameters and a DTM from which topographic variables are calculated. These variables are taken into account for estimation of radiation values: elevation, slope and azimuth. This allows obtaining incident solar radiation values on each point of the area and for a determined period. In areas without direct and diffuse radiation measures, which is usual in complex topography areas, it is not possible to calculate  $K$  and  $\tau$  values directly. Then, a procedure becomes necessary to split the global radiation into direct and diffuse components. This work intends to solve these questions in order to make the use of Solar Analyst more general.

For this target, we used a DTM with 20 m resolution and two radiometric station networks located in several zones. Both areas have a complex topography. We investigated a procedure to obtain  $K$  and  $\tau$  in the first area, and we have validated it with the second one. After that, we generated the daily solar radiation and its components in the second area with Solar Analyst, and the results have been compared with the measured data. Finally, a global radiation map has been estimated for the second area.

## 2. Experimental data

Two stations networks located in the south of Spain have been used. One of them is located in the Sierra Mágina Natural Park. It is composed of 11 stations with an extension of 2000 km<sup>2</sup> approximately. Ten stations have registered radiation data continuously since February 2005. The eleventh station corresponds to Jaén: it is a reference station where, since 2001, direct, diffuse and global radiation data are measured by means of one pyrheliometer and two pyranometers, KIPP-ZONEN, and two sensors, LICOR 200-SZ. Besides, spectral solar radiation measures are being registered, apart from other meteorological variables as pressure, temperature, wind speed and direction and relative humidity. The measures were integrated in a daily basis to obtain the daily global irradiation.

The second network is composed of 14 radiometric stations and is located in the north face of the Sierra Nevada Natural Park, in the Huéneja municipal district (Granada). Global solar irradiance data are registered with LICOR 200-SZ sensors. The measurements were integrated in a daily basis to obtain the daily global irradiation. Measurements used in this work include those registered between March 2003 and June 2005.

The calibration constants of the pyranometers are checked yearly, in all stations, against a reference Kipp and Zonen CM-11, reserved for this purpose and exposed to solar radiation only during these intercomparison campaigns.

Tables 1 and 2 show the characteristics of the stations: Universal Transverse Mercator (UTM) coordinates (where  $x$  stands for longitude and  $y$  for latitude), altitude, hillside slope and azimuth for both networks.

In the Mágina network, station altitudes range from 560 m to 2050 m above sea level with different slopes (from 0° to 30°) and azimuths. In the Huéneja network, station altitudes range from 1091 m to 1659 m; slope varies from 0° at station 13 to 19° at station 9; and azimuths range from 3° (north) at station 13 to 192° (south) at station 14.

Figs. 1 and 2 show the spatial distribution of the stations over a topographic map of the areas.

Table 1  
Stations location; altitude, slope and azimuth of hillsides corresponding to network 1

Station (number)	Longitude (U.T.M.)	Latitude (U.T.M.)	Altitude (a.m.s.l.)	Slope (°)	Azimuth (°)
1	431449	4182555	443	0	0
2	445994	4182267	762	5	340
3	453651	4176488	2015	18	180
4	456075	4181509	1075	25.5	250
5	458374	4183146	854	30	120
6	463612	4185316	634	15	250
7	464033	4182776	616	15	75
8	467059	4175098	704	16	110
9	460302	4167146	975	10	160
10	450121	4170107	728	15	120
11	443247	4177089	791	14.5	170

Table 2  
Stations location; altitude, slope and azimuth of hillsides corresponding to network 2

Station (number)	Longitude (U.T.M.)	Latitude (U.T.M.)	Altitude (a.m.s.l.)	Slope (°)	Azimuth (°)
1	502130	4111284	1659	10	150
2	502243	4111212	1669	14	192
3	502532	4111109	1619	13	177
4	502334	4111674	1558	9	116
5	502639	4111461	1565	5	83
6	502905	4111461	1532	11	152
7	503062	4111460	1505	3	82
8	503325	4111154	1467	19	180
9	503111	4111107	1449	19	85
10	503539	4112190	1305	5	40
11	503828	4112280	1292	15	68
12	503658	4112414	1300	8	106
13	505529	4114325	1188	0	3
14	508391	4116254	1091	6	153

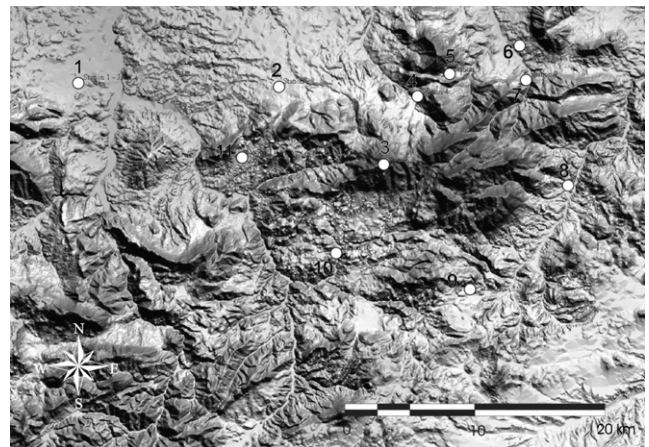


Fig. 1. Stations distribution on a topographic map of the first region.

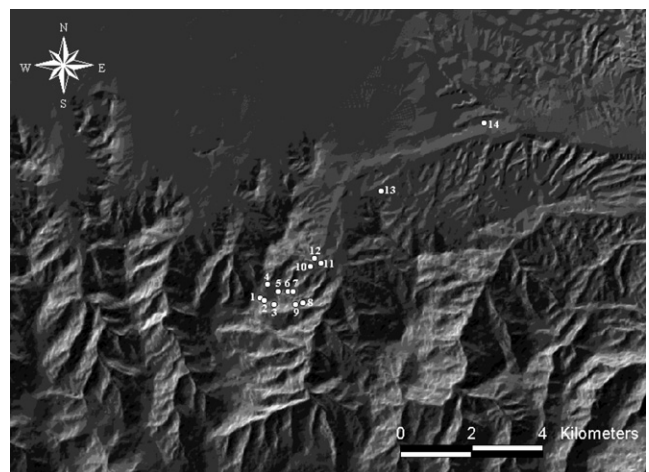


Fig. 2. Stations distribution on a topographic map of the second region.

## 3. Methodology

Solar radiation originating from the sun travels through the atmosphere. The amount of solar radiation

on the surface depends on the topography and surface features. The topographic characteristics can modify the direct, diffuse and reflected components collected in a site. Generally, direct solar radiation is the largest component of global solar radiation, and diffuse solar radiation is the second largest component. Solar radiation reflected to a location from surrounding topographic features often accounts for a small proportion of the total incident radiation and, for many purposes, can be neglected [16–21].

In this paper, we estimate the daily global radiation using the algorithms by Fu and Rich implemented in Solar Analyst [22,23] as an ArcView GIS [24] extension that calculates the direct and diffuse components of solar radiation, just as the number of sunshine hours based on a DTM, the diffuse fraction  $K$  and the atmospheric transmittivity,  $\tau$ .

Solar Analyst can use default  $K$  and  $\tau$  values corresponding to clear sky, but to obtain actual radiation maps of a zone it is necessary to estimate average values of  $K$  and  $\tau$  for every kind of sky conditions. From the different ranges of the clearness index  $k_t$  (daily global irradiation/daily extraterrestrial irradiation), it is possible to characterize the state of the sky [25–28]. The daily clearness index gives information about the amount of clouds in the atmosphere in such a way that high  $k_t$  values are associated with clear skies whereas low values are related to cloudy skies. The diffuse fraction contains information about atmospheric turbidity, low  $K$  values being associated with clean skies and high values of diffuse fraction being linked to high turbidity.

In a first stage, a preliminary study has been made to characterize the sky state. We have differentiated the sky according to four  $k_t$  intervals ( $k_t < 0.35, 0.35 < k_t < 0.55, 0.55 < k_t < 0.65, k_t > 0.65$ ), and monthly means of daily  $K$  and  $\tau$  were calculated for each interval from the global irradiation values. The daily diffuse fraction was obtained from data measured in the radiometric network in Sierra Mágina, and these results have been applied later to the Sierra Nevada network in order to be independent of

the data analyzed. The correlation obtained between  $K$  and  $k_t$  is given by the following equation:

$$K = \begin{cases} 0.97 & \text{for } k_t \leq 0.18 \\ 0.99 - 0.356k_t + 2,783k_t^2 - 10.67k_t^3 + 7.63k_t^4 & \text{for } k_t > 0.18 \end{cases} \quad (1)$$

Atmospheric transmittivity  $\tau$ , was obtained using the calculated diffuse fraction and the global solar radiation measurements. In Table 3, estimated values for  $K$  and  $\tau$  are shown for each month of the year as a function of the clearness index  $k_t$ . These values have been utilized in this work as inputs for Solar Analyst.

To estimate direct and diffuse solar radiation, the model creates a shadow map, a sky map and a sun track map. Now, we describe the main features of the methodology utilized for calculating daily global radiation [23].

Viewsheds are the angular distribution of sky visibility versus obstruction. This is similar to the view provided by upward looking hemispherical (fish eye) photographs. A viewshed is calculated by searching in a specified set of directions around a location of interest, determining the maximum angle of obstruction, sometimes referred to as effective horizon angle, in each direction.

Sky maps are raster maps constructed by dividing the whole sky into a series of sky sectors defined by zenith and azimuth divisions. The zenith and azimuth angles of the centroid of each sector are calculated. Sky sectors must be small enough that the centroid zenith and azimuth angles reasonably represent the direction of the sky sector in subsequent calculations.

The sun track map consists of a raster representation that specifies sun tracks, the apparent position of the sun as it varies through time. In particular, sun tracks are represented by discrete sky sectors, defined by the sun position at intervals through the day and season. For each sector, the associated time duration and the azimuth and zenith at its centroid are calculated.

The viewshed is overlaid on the sky map and the sun map (as it appears in Figs. 3 and 4 for stations 9 and 14, respectively), to enable calculation of the diffuse and direct

Table 3  
Monthly values for diffuse fraction and atmospheric transmittivity

	$k_t < 0.35$		$0.35 < k_t < 0.5$		$0.5 < k_t < 0.65$		$0.65 < k_t$	
	$k$	$\tau$	$k$	$\tau$	$k$	$\tau$	$k$	$\tau$
January	0.944	0.073	0.753	0.301	0.466	0.532	0.276	0.678
February	0.944	0.058	0.734	0.266	0.492	0.468	0.260	0.679
March	0.942	0.043	0.756	0.210	0.476	0.458	0.264	0.654
April	0.940	0.034	0.746	0.194	0.469	0.431	0.249	0.648
May	0.931	0.039	0.708	0.211	0.457	0.429	0.254	0.631
June	0.832	0.092	0.670	0.242	0.447	0.436	0.279	0.595
July	0.855	0.082	0.790	0.144	0.442	0.442	0.270	0.612
August	0.853	0.107	0.724	0.222	0.381	0.503	0.274	0.607
September	0.946	0.037	0.739	0.221	0.425	0.491	0.258	0.659
October	0.948	0.052	0.704	0.297	0.470	0.497	0.269	0.666
November	0.929	0.104	0.734	0.305	0.428	0.563	0.284	0.678
December	0.944	0.088	0.678	0.378	0.445	0.561	0.294	0.680

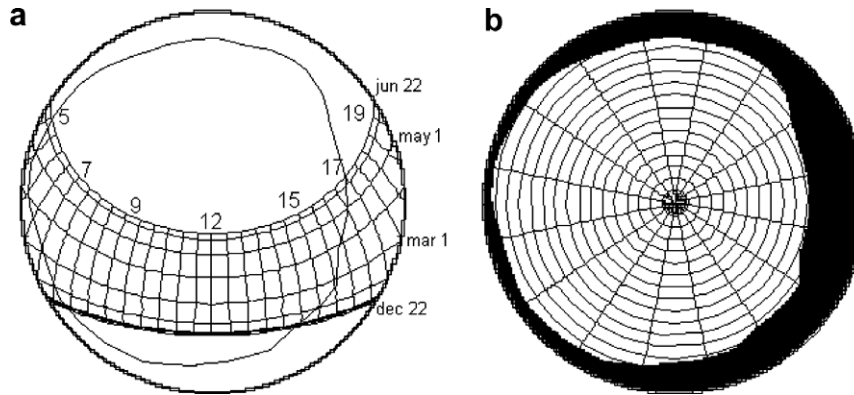


Fig. 3. Viewshed overlaid on a sun map (a) and a sky map (b) for station 9. Shaded areas are obstructed sky directions.

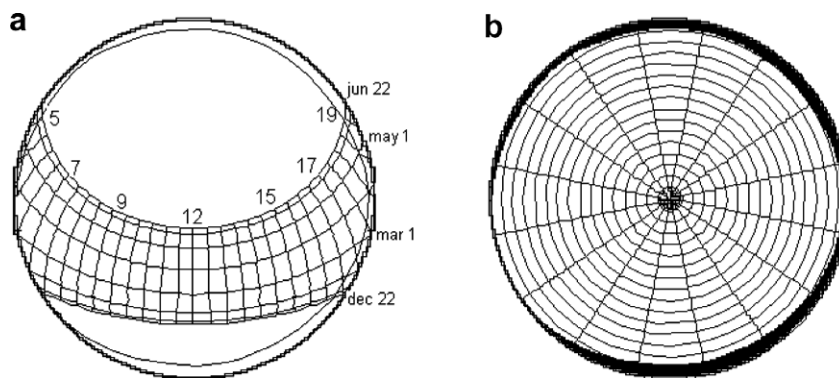


Fig. 4. Viewshed overlaid on a sun map (a) and a sky map (b) for station 14. Shaded areas are obstructed sky directions.

radiation received from each sky direction. Shaded areas are obstructed sky directions. Gap fraction, the proportion of unobstructed sky area in each sky map or sun map sector, is calculated by dividing the number of unobstructed cells by the total number of cells in that sector.

### 3.1. Direct solar radiation calculation

For each sun map sector that is not completely obstructed, direct solar radiation is calculated based on the gap fraction, sun position, atmospheric attenuation and ground receiving surface orientation of the intercepting surface. The Solar Analyst implements a simple model [16–18,29,30], which starts with the solar constant and accounts for atmospheric effects based on transmittivity and air mass depth.

Daily direct radiation,  $H_b$ , for a ground location, is the sum of the direct radiation ( $B_{\theta_z, \psi}$ ) from all sun map sectors:

$$H_b = \sum B_{\theta_z, \psi} \quad (2)$$

$$B_{\theta_z, \psi} = I_{sc} \tau^{m\theta} S_{\theta_z, \psi} \zeta_{\theta_z, \psi} \cos(\theta) \quad (3)$$

$$\theta = a \cos[\cos(\theta_z) \cos(\theta_s) + \text{sen}(\theta_z) \text{sen}(\theta_s) \cos(\psi - \psi_s)] \quad (4)$$

### 3.2. Diffuse solar radiation calculation

For diffuse radiation, the uniform diffuse model and the standard overcast diffuse model are typically imple-

mented [17,18,29] with satisfactory results. In a uniform diffuse model, sometimes referred to as “uniform overcast sky” but often applied in clear sky conditions, incoming diffuse radiation is assumed to be the same from all sky directions. In a standard overcast diffuse model, diffuse solar radiation flux varies with zenith angle according to an empirical relation [31]. Both models are implemented in the Solar Analyst. For each sky sector, the diffuse solar radiation at its centroid  $D_{\theta_z, \psi}$  is calculated. Daily diffuse solar radiation,  $H_d$ , for the location, is calculated as the sum of the diffuse solar radiation from all the sky map sectors

$$H_d = \sum D_{\theta_z, \psi} \quad (5)$$

$$D_{\theta_z, \psi} = R_n K \Delta V_{\theta_z, \psi} S_{\theta_z, \psi} \cos(\theta) \quad (6)$$

### 3.3. Global solar radiation calculation

Global solar radiation  $H_g$  is calculated as the sum of direct and diffuse radiation of all sectors.

$$H_g = H_b + H_d \quad (7)$$

The above calculation of viewshed, overlay of viewshed on sun maps and sky maps, and calculation of direct, diffuse and global radiation, is repeated for each location on the topographic surface, thus producing radiation maps for an entire geographic area.

4. Results and discussion

The global solar radiation behavior has been analyzed as a function of altitude, hillside slope and azimuth. After this, we have estimated global solar radiation with the algorithms by Fu and Rich [22] and the estimated values are compared with the measured ones.

Table 4 shows the monthly and annual values of measured global solar radiation for each of the stations of network 2. From analysis of the annual values, we observe that there is not a clear dependence between global solar radiation and the topographic variables: altitude, slope and azimuth. However, a slight attenuation tendency is observed in the radiation for the higher stations. This result is unexpected since global radiation typically increases 8% for every 1000 m of height above mean sea level [32]. We think that in the current microclimate present in the zone, elevation differences are less important than other topographic variables, like the shadows produced by adjacent mountains. Considering the potential annual sunshine hours, a close relation with the incoming solar radiation is observed. Station 14 is the one with the largest number of hours and the major radiation levels, with values of 4189 h and 6296 MJ/m<sup>2</sup>. On the other hand, station 9 is the one with the lowest annual values for both irradiation (5910 MJ/m<sup>2</sup>) and sunshine hours (3416 h).

We emphasize that station 14 has the lowest elevation (1091 m) and station 9 a mid elevation (1449 m). As we have already pointed out, the topography effect on the energy balance is essential, Fig. 3 represents the station 9 viewshed and Fig. 4 shows the viewshed for station 14 in conjunction with their sun map and sky map. In station 14, a minimum horizon obstruction is observed, whereas in station 9, the horizon has a larger effect. More important than the amount of obstruction is its angular distribution. As it is observed, station 9 shows a large obstruction along the west, which makes this station the one with less radiation even if it is located at a medium elevation. The obstruction in the north direction does not affect the arriv-

ing radiation because the topography does not intersect the sun path. It is also interesting to note that station 14 is placed in a flat area while station 9 is in a gully. Analyzing monthly values, as could be expected, it is observed that the maximum values correspond to summer months and the minimum to winter months for all the stations. The mentioned values range from 220 MJ/m<sup>2</sup> in December to 830 MJ/m<sup>2</sup> in July.

We have estimated the daily global solar radiation in the complex topography area for all sky conditions by using a 20 m resolution DTM with Solar Analyst software (Fu and Rich [23]). The main input variables of those algorithms are the atmospheric transmittivity  $\tau$ , and the daily diffuse fraction  $K$ .

Statistical analysis results for every station and for each  $k_t$  interval are shown in Figs. 5 and 6 in terms of root mean square error (RMSE) and mean bias error (MBE) expressed as a percentage of the mean measured value on that interval. MBE gives information about a possible underestimation or overestimation performed by the global solar radiation model, and RMSE is linked to data dispersion.

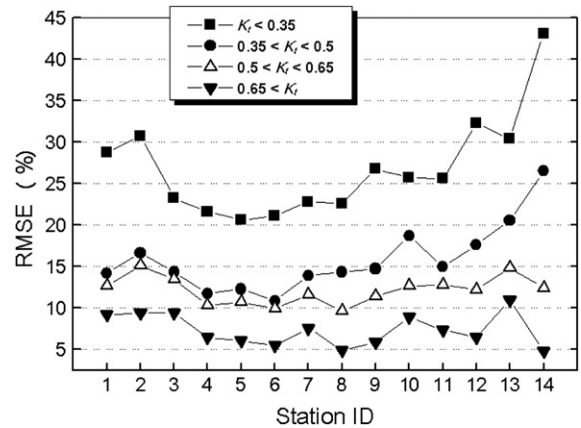


Fig. 5. Root mean square error, expressed as a mean measured value percentage, for each station.

Table 4 Annual and monthly global irradiation (MJ/m<sup>2</sup>); potential annual number of sunshine hours for every station (h)

ID	1	2	3	4	5	6	7	8	9	10	11	12	13	14
January	343	339	351	336	322	336	342	340	318	287	345	341	341	361
February	331	344	349	342	333	353	342	357	321	307	351	354	416	340
March	503	498	496	497	484	507	492	513	475	487	498	515	532	505
April	672	684	679	680	671	678	673	687	637	697	687	697	676	682
May	617	608	635	629	615	624	624	632	606	614	633	646	644	670
June	784	774	789	821	770	790	768	784	768	774	791	785	769	783
July	832	831	824	863	843	835	834	834	796	807	823	838	824	825
August	692	687	689	704	689	698	697	687	669	655	691	697	676	680
September	510	503	506	509	503	503	501	504	496	478	503	511	504	506
October	395	385	395	391	387	388	386	396	380	362	391	407	386	388
November	263	261	267	260	251	262	260	274	255	236	261	271	260	275
December	211	215	212	221	221	221	211	236	217	205	220	235	226	238
Year total	6154	6128	6193	6252	6088	6192	6128	6243	5936	5910	6194	6296	6252	6252
Sun hours	3849	3633	3970	3817	3875	3995	3902	3898	3416	3796	3844	3770	4154	4189

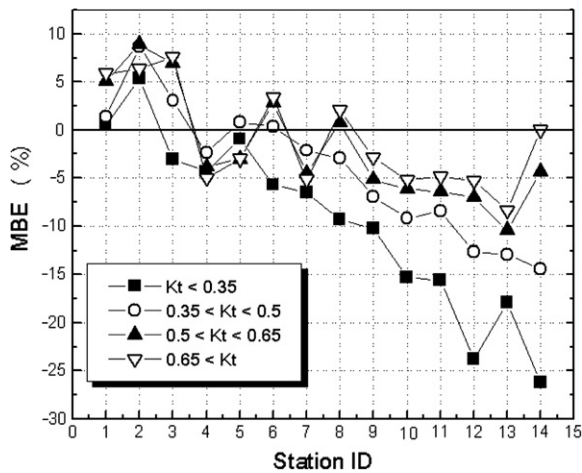


Fig. 6. Mean bias error, expressed as a mean measured value percentage, for each station.

$$MBE (\%) = \frac{\left( \frac{\sum (X_{estimated} - X_{measured})}{N} \right)}{\bar{X}_{measured}} \cdot 100 \quad (8)$$

$$RMSE (\%) = \frac{\left( \sqrt{\frac{\sum (X_{estimated} - X_{measured})^2}{N}} \right)}{\bar{X}_{measured}} \cdot 100 \quad (9)$$

For the  $k_t > 0.65$  interval, daily global solar irradiation of the upper stations (1, 2, 3) is overestimated by the model, whereas for the rest of stations, it is underestimated. The RMSE keeps under 11% for the whole station set. For the  $0.5 < k_t < 0.65$  interval, MBE values are very similar to those obtained for the first interval; in contrast, RMSE increases for all the stations, with a rise around 4%. For the  $0.35 < k_t < 0.5$  interval, RMSE increases around 7% with respect to the first considered interval. The last interval,  $k_t < 0.35$ , contains the largest errors, with a mean RMSE around 26%, which is a 16% increase compared to the  $k_t > 0.65$  interval. MBE also becomes considerably larger in regard to the rest of the intervals, showing a strong underestimation tendency. The RMSE increases when the clearness index decreases due to the fact that atmospheric transmittivity and diffuse fraction are not sufficient in order to characterize the influence of clouds on the solar radiation attenuation. It can be observed that the best performance is achieved for clear sky conditions ( $k_t > 0.65$ ) with a RMSE lower than 11% and MBE below 7%. This happens because, in this interval, the cloud influence over solar radiation is minimal, and therefore, solar radiation attenuation can be explained in terms of atmospheric transmittivity. Considering the complete  $k_t$  range, a RMSE less than 10% and, except for station 13, a MBE lower than 7% is observed.

Table 5  
Statistical analysis of the measured and estimated values, for each station

	January	February	March	April	May	June	July	August	September	October	November	December	Total
<b>MBE (%)</b>													
1	13.72	11.16	7.09	2.11	0.26	-2.10	-0.08	1.39	6.70	3.98	13.65	24.90	4.73
2	14.57	12.29	12.81	4.49	2.88	-0.94	0.96	3.68	10.05	9.06	17.85	25.58	7.38
3	10.23	7.98	9.37	4.58	0.39	1.06	3.70	4.40	9.02	4.52	13.99	24.82	6.26
4	-14.49	-9.35	-2.69	-3.13	-0.93	-3.79	-2.07	-3.55	-2.77	-8.55	-6.96	-3.93	-4.31
5	-12.54	-9.09	-1.28	-1.37	0.60	0.99	-0.41	-1.14	-2.63	-7.54	-4.12	-5.20	-2.48
6	4.40	0.20	2.86	1.06	1.76	0.01	2.83	1.46	6.01	0.81	5.77	10.99	2.38
7	-18.62	-11.49	-4.57	-3.70	-2.09	-0.42	-0.29	-3.82	-3.54	-9.33	-8.57	-2.43	-4.66
8	0.37	-3.00	0.08	-0.35	0.04	-0.25	2.84	3.37	4.54	-3.31	0.87	1.08	0.42
9	-12.57	-7.54	-3.31	-1.18	-4.21	-4.17	0.83	-1.46	-6.24	-11.84	-10.85	-8.85	-4.50
10	-12.11	-14.39	-12.64	-10.15	-2.26	-1.89	2.25	3.46	-2.73	-8.83	-10.66	-7.84	-6.52
11	-19.80	-14.79	-7.49	-5.34	-3.85	-3.24	1.66	-2.52	-4.35	-12.22	-10.91	-8.04	-6.36
12	-12.50	-11.97	-9.39	-8.18	-7.56	-4.31	-2.15	-4.73	-5.28	-14.48	-9.83	-10.56	-7.73
13	-28.09	-21.33	-12.73	-8.37	-7.35	-1.45	-0.63	-2.38	-9.67	-16.96	-18.61	-18.65	-10.10
14	-11.27	-8.76	-7.47	-3.96	-8.99	-2.29	1.05	1.00	-1.58	-5.36	-5.47	-8.06	-4.70
<b>RMSE (%)</b>													
1	20.87	16.72	15.12	6.73	9.51	6.68	5.04	5.20	10.44	13.63	18.93	43.25	11.83
2	19.88	16.65	17.72	7.91	10.71	6.93	5.31	6.88	12.60	16.85	22.99	43.80	13.11
3	17.18	14.07	16.32	8.20	8.33	6.39	5.90	5.96	12.18	13.53	19.27	45.97	12.10
4	15.51	12.69	9.66	7.15	8.57	7.11	6.40	6.20	9.15	11.94	12.27	13.88	9.17
5	15.95	12.50	9.54	7.44	9.24	5.94	6.61	7.74	8.72	11.63	10.34	14.12	9.14
6	10.49	9.10	10.50	6.64	9.47	5.52	5.26	4.52	9.83	9.92	11.26	19.81	8.48
7	23.19	14.78	11.11	8.38	9.07	5.65	4.34	9.22	8.68	13.00	13.99	25.93	10.46
8	9.01	9.98	10.96	7.19	8.90	5.58	5.19	5.40	9.04	11.47	12.42	20.63	8.78
9	14.92	13.68	10.28	7.97	9.90	6.74	4.89	6.82	9.52	14.37	15.51	23.24	9.94
10	13.71	18.03	16.91	12.72	10.28	5.67	5.98	8.76	7.68	11.76	16.34	18.92	12.31
11	20.89	17.21	11.61	8.91	10.54	9.03	4.71	9.32	9.32	14.95	14.07	13.28	11.19
12	14.71	14.68	13.63	10.52	12.07	7.95	4.85	6.38	10.15	16.88	13.54	20.08	11.39
13	28.44	22.89	18.16	11.45	12.86	6.03	4.72	7.47	13.32	19.08	23.48	26.30	14.59
14	15.51	18.77	19.23	11.43	16.73	5.62	4.67	5.73	8.96	18.17	18.01	23.26	13.57

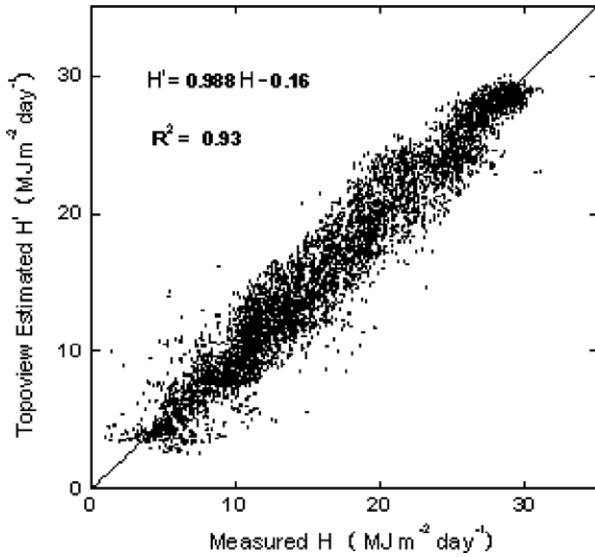


Fig. 7. Scatter plot of estimated daily global irradiation versus measured daily global irradiation for the whole stations set.

Table 5 contains the statistical analysis results for each station and for every month, and changes in the RMSE and MBE are reported. Daily global radiation is overestimated for the highest stations (1, 2, 3) along the whole year, whereas it is underestimated for the rest of stations. The best results are observed during the summer months and the worst performance takes place in winter months. Percentage errors reach the minimum in July and become maximal in

December. For July, all the stations have a RMSE and MBE under 6% and 4%, respectively. On the contrary, December shows a RMSE over 21% for the whole station set; and a global tendency to underestimate. In regard to the annual values, the RMSE is around 11% and MBE is under 7%, with the exception of station 10. Fig. 7 shows, for the whole data set, the model estimates versus measured global radiation. Values lower than 10 MJ/(m<sup>2</sup> day) are usually overestimated as can be observed from the fact that many points are located above the 1:1 fit line; a larger dispersion of the points is also observed in the same region. In contrast, for daily global irradiation values over 25 MJ/(m<sup>2</sup> day), the data dispersion is minimal and most of the points are on the perfect fit line 1:1.

Once the Solar Analyst performance has been analyzed and in view of the satisfactory results provided in the global radiation estimates for the 14 stations located on a complex topography area, we consider the generation of a map with annual radiation values for the zone. To obtain the mentioned map, we have used a DTM of the area with a size of (18 × 18) km<sup>2</sup> and a resolution of 20 m, covering a 324 km<sup>2</sup> surface. The annual global solar radiation map is shown in Fig. 8. It is interesting to note that the studied area has been remarkably increased.

Considering elevation, the annual radiation levels lie around 6000 MJ/(m<sup>2</sup> year) for the lowest zones and around 7000 MJ/(m<sup>2</sup> year) for the higher elevations. On the other hand, the lowest irradiation levels are reported to be around 3000 MJ/(m<sup>2</sup> year), and they are found in very abrupt

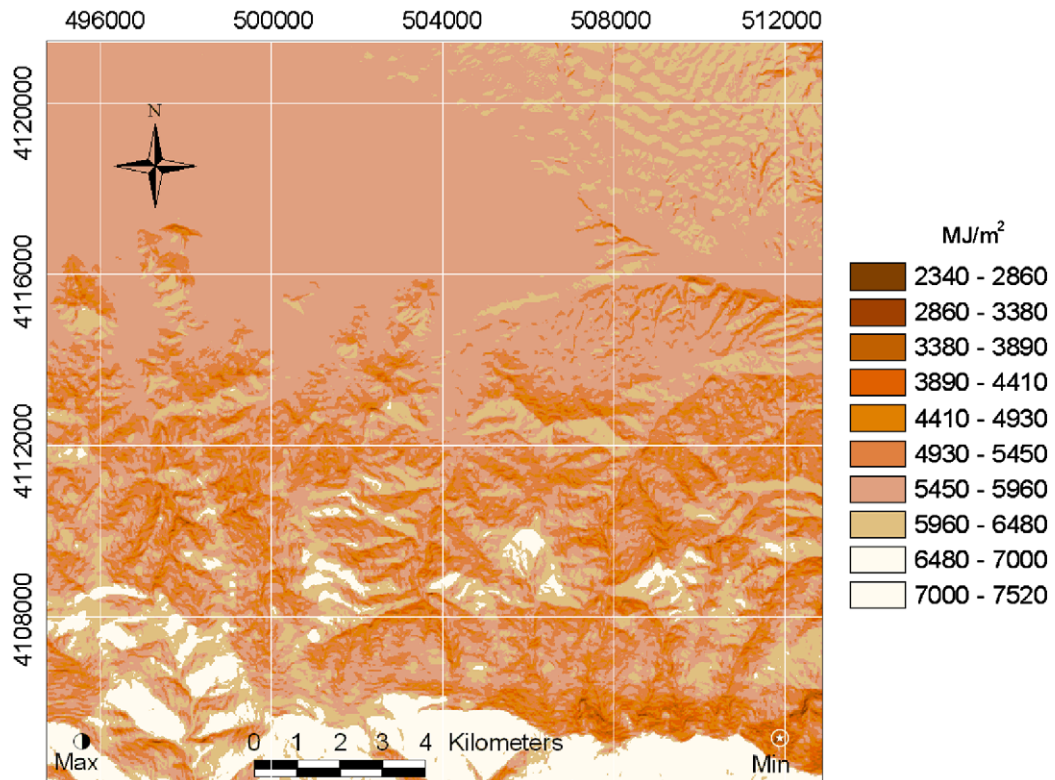


Fig. 8. Annual global irradiation map for the studied zone.

regions. Therefore, irradiation levels are more related to the topographic characteristics of the studied area than to the altitude. Maximum and minimum annual values were reported to be 7516 MJ/(m<sup>2</sup> year) and 2342 MJ/(m<sup>2</sup> year). The maximum location is described by (495426, 4105360) UTM coordinates; 2595 m altitude; 21.19° slope; and 178.15° (~south) azimuth, and the minimum is described by (511786, 4105120) UTM coordinates; 2153 m altitude; 61.48° slope; and 337.01° (~north) azimuth.

One of the most important limitations of the Solar Analyst resides in the requirement of the inputs  $K$  (diffuse fraction) and  $\tau$  (atmospheric transmittivity). The model is easy to apply when those index values are well known, but this only happens in extreme conditions, like very clear or totally covered skies. A close relation between model performance and the ( $K, \tau$ ) values introduced has been observed in this work. If the pair of values ( $K, \tau$ ) is inadequate, the errors obtained can increase, with the RMSE above 60%. To obtain those indices for all sky conditions, global and diffuse radiation measures are needed. We are working on the use of satellite images to estimate  $K$  and  $\tau$  in places where no radiometric measurements are being made. Satellite images have a wide spatial and temporal coverage, but low spatial resolution when dealing with pixels with a strong topographic gradient. We think that by combining the use of DTMs and satellite images, estimates of global solar radiation over complex topography sites will be improved.

## 5. Conclusions

In this paper, we have firstly analyzed the influence of topographic parameters (elevation, slope and azimuth) on the measured global solar radiation. We have found that the main variables driving the insolation levels on a mountainous surface are the azimuth and the horizon effect (obstruction due to horizon) with altitude becoming a secondary relevant parameter. The station receiving less levels of radiation is the one with a more obstructed horizon.

A correlation between  $k_t$  and  $K$  has been obtained, and it allows getting the diffuse fraction and the transmittivity from horizontal global radiation measures in a complex topography area.

Afterwards, daily global solar radiation has been estimated under all sky conditions for 14 stations located in a complex topography site using the Solar Analyst software and a (20 × 20) m DTM. A seasonal dependence of the model is observed. The best results are achieved during the summer months and the worst results during winter. In particular, errors become lowest in the month of July and largest during December. In July, all the stations give RMSE and MBE values below 6% and 4%, respectively. On the contrary, in December, RMSE is over 21% for all the stations, and there is also a general tendency toward underestimation. The RMSE averages for the whole year are below 11% for all the stations and the averaged MBE is less than 7%, except for station 10. The dependence between the results provided by the model and diffuse frac-

tion ( $K$ ) and atmospheric transmittivity ( $\tau$ ) values has also been reported. If the pair of values ( $K, \tau$ ) introduced to the model is inadequate, the errors obtained become very high, with RMSE even above 60%. In this work,  $K$  and  $\tau$  were estimated for the studied area.

Finally, evaluating the global solar irradiation, an annual irradiation map has been obtained for a 324 km<sup>2</sup> area containing the radiometric network, and a tight relation of irradiation with topography has been reported. Several areas with a very high elevation are observed to have a minimum annual irradiation level. On the contrary, there are very low areas where the annual global irradiation is higher than 5750 MJ/m<sup>2</sup>.

## Acknowledgements

This work has been accomplished thanks to the project ENE-2004-07816-C03-01 funded by the Ministerio de Ciencia y Tecnología of Spain. Authors are also grateful to Adrien Roby for his help with the generation of the radiation maps.

## References

- [1] Jacobson MZ. *Fundamentals of Atmospheric Modeling*. Cambridge University Press; 1999.
- [2] Berninger F. Simulated irradiance and temperature estimates as a possible source of bias in the simulation of photosynthesis. *Agric Forest Meteorol* 1994;71:19–32.
- [3] Suehrcke H, McCormick PG. Solar radiation utilizability. *Sol Energy* 1989;43:339–45.
- [4] Suehrcke H, McCormick PG. Performance prediction method for solar energy systems. *Sol Energy* 1992;48:169–75.
- [5] Tovar J, Olmo FJ, Alados-Arboledas L. Local scale variability of solar radiation in mountainous region. *J Appl Meteorol* 1995;34:2316–22.
- [6] Tovar J, Olmo FJ, Batlles FJ, Alados-Arboledas L. One minute kb and kd probability density distributions conditioned to the optical air mass. *Sol Energy* 1999;65:297–304.
- [7] Mariscal MJ, Orgaz F, Villalobos FJ. Modelling and measurement of radiation interception by olive canopies. *Agric Forest Meteorol* 2000;100:183–97.
- [8] Hansen JW. Stochastic daily solar irradiance for biological modeling applications. *Agric Forest Meteorol* 1999;94:53–63.
- [9] Pinker RT, Laszlo I, Goodrich D, Pandithurai G. Satellite estimates of surface radiative fluxes for the extended San Pedro Basin: sensitivity to aerosols. *Agric Forest Meteorol* 2000;105:43–54.
- [10] Duguay CR. Radiation modeling in mountainous terrain: review and status. *Mt Res Dev* 1993;13:339–57.
- [11] Dubayah R, Loechel S. Modeling topographic solar radiation using GOES data. *J Appl Meteorol* 1997;36:141–54.
- [12] Baker DG, Skaggs RH. The distance factor in the relationships between solar radiation and sunshine. *J Climatol* 1984;4:123–32.
- [13] Long CN, Ackerman TP. Surface measurements of solar irradiance: a study of the spatial correlation between simultaneous measurements at separated sites. *J Appl Meteorol* 1995;34:1039–46.
- [14] Zelenka A, Czeplak G, d'Agostino V, Josefson W, Maxwell E, Perez R. Techniques for supplementing solar radiation network data. Technical Report, International Energy Agency; 1992.
- [15] Dubayah R, van Katwijk V. The topographic distribution of annual incoming solar radiation in the Rio Grande River Basin. *Geophys Res Lett* 1992;19:2231–4.

- [16] Gates DM. Biophysical ecology. New York: Springer-Verlag; 1980.
- [17] Rich PM. A manual for analysis of hemispherical canopy photography. Los Alamos National Laboratory Report; 1989, LA-11733-M.
- [18] Rich PM. Characterizing plant canopies with hemispherical photography. In: Goel NS, Norman JM, editors. Instrumentation for studying vegetation canopies for remote sensing in optical and thermal infrared regions. Remote Sensing Rev 1990;5:13–29.
- [19] Hetrick WA, Rich PM, Barnes FJ, Weiss SB. GIS-based solar radiation flux models. American Society for Photogrammetry and Remote Sensing Technical Papers. GIS, Photogramm Model 1993;3:132–43.
- [20] Hetrick WA, Rich PM, Weiss SB. Modeling insolation on complex surfaces. In: Thirteenth annual ESRI user conference, vol. 2; 1993. p. 447–58.
- [21] Kumar L, Skidmore AK, Knowles E. Modelling topographic variation in solar radiation in a GIS environment. Int J Geogr Inf Sci 1997;11:475–97.
- [22] Fu P, Rich PM. Design and implementation of the Solar Analyst: an ArcView extension for modeling solar radiation at landscape scales. In: Proceedings of the 19th annual ESRI user conference, San Diego, USA; 1999.
- [23] Fu P, Rich PM. The Solar Analyst user manual. Helios Environmental Modeling Institute, LLC, Vermont; 2000.
- [24] Arc View GIS 3.2. Environmental Systems Research Institute Inc.; 1999.
- [25] Orgill JF, Hollands KGT. Correlation equation for hourly diffuse radiation on a horizontal surface. Sol Energy 1977;19:357–9.
- [26] Iqbal M. Prediction of hourly diffuse solar radiation from measured hourly global radiation on a horizontal surface. Sol Energy 1980;24:491–503.
- [27] Erbs DG, Klein SA, Duffie JA. Estimation of the diffuse radiation fraction for hourly, daily and monthly average global radiation. Sol Energy 1982;28:293–302.
- [28] Reindl DT, Beckman WA, Duffie JA. Diffuse fraction correlations. Sol Energy 1990;45:1–7.
- [29] Pearcy RW. Radiation and light measurements. In: Pearcy RW, Ehleringer JR, Mooney HA, Rundel PW, editors. Plant physiological ecology: field methods and instrumentation. New York: Chapman & Hall; 1989. p. 95–116.
- [30] List RJ. Smithsonian meteorological tables. 6th revised ed. Smithsonian miscellaneous collection, vol. 114. Washington: Smithsonian Institution Press; 1971.
- [31] Moon P, Spencer DE. Illumination from a non-uniform sky. Trans Illum Eng Soc NY 1942;37:707–26.
- [32] Blumthaler M, Ambach W, Ellinger R. Increase in solar UV radiation with altitude. J Photochem Photobiol 1997;39:130–4.